Transforming Nature's Bath Sponge into Stacking Faults Enhanced Ag Nanorings Decorated Catalyst for Hydrogen Evolution Reaction

Chirag R. Ratwani[a], Shadeepa Karunarathne[a], Ali Reza Kamali[b,c*], Amr M. Abdelkader[a*]

[a]*Department of Design and Engineering, Faculty of Science & Technology, Bournemouth University, Poole, Dorset BH12 5BB, United Kingdom*

[b]*Energy and Environmental Materials Research Centre (E2MC), School of Metallurgy, Northeastern University, Shenyang 110819, China*

[c]*Department of Materials Science and Metallurgy, University of Cambridge, Cambridge CB3 0FS, United Kingdom*

Keywords: Hydrogen evolution reaction, Stacking fault, Silver, Electrocatalysis, Biomass based catalysts, Carbonization

*Corresponding authors: Amr M. Abdelkader, email: aabdelkader@bournemouth.ac.uk

Ali Reza Kamali, email: ali@mail.neu.edu.cn

Abstract

The rational design of cost-effective and efficient electrocatalysts for electrochemical water splitting is essential for green hydrogen production. Utilisation of nanocatalysts with abundant active sites, high surface area and deliberate stacking faults is a promising approach to enhancing catalytic efficiency. In this study, we report a simple strategy to synthesise a highly efficient electrocatalyst for the hydrogen evolution reaction (HER) using carbonised luffa cylindrica as a conductive N-doped carbon skeleton decorated with Ag nanorings that are activated by introducing stacking faults. The introduction of stacking faults and the resulting tensile strain into the Ag nanorings results in a significant decrease in the HER overpotential, enabling the use of Ag as an efficient HER electrocatalyst despite its low intrinsic activity. Our findings demonstrate that manipulating the crystal properties of electrocatalysts, even for materials with intrinsically poor catalytic activity, such as Ag, can result in highly efficient catalysts. Further, applying a conductive carbon backbone can lower the quantities of metals needed without compromising the HER activity. This approach opens new avenues for designing high-performance electrocatalysts with very low metallic content, which could significantly impact the development of sustainable and cost-effective electrochemical water-splitting systems.

Introduction

The world's increasing population and economic development escalate the demand for global energy. Hydrogen, with its versatility as a feedstock in chemical processes and as a clean energy carrier, stands out to meet this rising energy demand. [1] However, most of the hydrogen produced to date is by cracking of hydrocarbon gases, thereby making it reliant on fossil fuels.[2] To reduce the carbon footprint and produce high-purity hydrogen, green methods like electrocatalytic water splitting from water have gained attention.[3] The success of this strategy significantly depends on the electrocatalysts' performance facilitating the Oxygen Evolution Reaction (OER) and the Hydrogen Evolution Reaction (HER) during water splitting. The ideal electrocatalysts should boast high catalytic activity and conductivity, low cost, easy processability, and high stability.[4-6] Traditional bulk metal catalysts often underutilize active sites, leading to reduced mass activity due to insufficient electrolyte contact.[7] Currently, the most effective HER catalysts are composites of platinum metal, with the leading contender being the state-of-the-art Pt/C catalyst. The excellent performance of Pt/C is attributed mainly to the d9 electronic structure of Pt that allows ready adsorption of intermediates obtained by HER onto the Pt surface. The Pt component of this composite catalyses the HER based on the Sabatier principle, and it is further supported by the conductive surface of the carbon catalyst support to improve electron transfer.[8] The main constraint with using Pt-based catalysts is the high cost and limited availability of Pt in nature.[9]

Cheaper noble metals like Ag offer high conductivity but exhibit weak hydrogen adsorption and, subsequently, poor HER activity due to their d10 electronic structure. [5, 10] Therefore, structural changes are required to enhance the adsorption of reactants/intermediates on the Ag sites and, consequently, the catalytic behaviour.[11] Various strategies have been used to improve the performance of catalysts for HER reaction; for example, reducing the particle size to increase the available active surface area and allow for more efficient adsorption/desorption. [12, 13] Another approach to improving the intrinsic activity of metal catalysts is to modify their electronic properties.[14, 15] It is also very well known that when carbon materials are combined with metal catalysts, significant improvement in the catalytic properties can be achieved. This synergy arises from the increased electrochemically active

surface area, which enhances hydrogen adsorption, increases the mechanical stability of nanoparticles, and provides an efficient pathway for electron transfer, as demonstrated elsewhere.[16-20] From economic and practical points of view, it would be ideal to utilise less expensive metal nanoparticles with crystal structures suitable for H_2 adsorption integrated into heterostructure along with a high surface area conductive carbon matrix.

Recent studies have reported that crystal defect sites can strongly affect the conductivity and catalytic performance of the electrocatalysts.[21, 22] The main reason is that the atoms at the surface of stacking faults have a lower number of neighbours (coordination number) than those in the bulk material, and they can also experience significant lattice strain.[23] Both of these factors can alter the electronic properties of the atoms, which can, in turn, affect their ability to adsorb and activate reactants.[24] Earlier research has focused on introducing stacking faults into the crystal structure of metal nanoparticles as a means to improve the hydrogen adsorption performance.[25] Such crystalline defects can also provide a significant effect in transforming materials that are basically inactive for the hydrogen evolution reaction into effective catalysts.[26] For example, Ramadhan et al. explored the effect of stacking faults on enhancing the catalytic activity of Ni nanoparticles for improved electrocatalytic oxidation of 5-hydroxymethylfurfural.[27] Ru nanoparticles with abundant stacking faults have also been explored for improved electrocatalytic water splitting, yielding an overpotential of 196 and 35 mV for OER and HER at 10 mA/cm^2, respectively. [28] In another work using laser ablation, researchers took advantage of the silver's low stacking fault energy and created Ag nanoparticles with a 5.7% tensile strain.[26] These Ag nanoparticles exhibited superior performance and stability during the HER, surpassing the current standard Pt/C benchmark. Theoretical calculations in the mentioned study have also shown a remarkable reduction in the hydrogen absorption Gibbs free energy, ultimately responsible for excellent catalyst performance.

Motivated by the potential of Ag as an effective electrocatalyst, we demonstrate a low-cost method for synthesizing a silver-based high-strain catalyst and support system with improved HER performance. This structure consists of a minimal amount of Ag nanorings serving as a metal catalyst, loaded onto biomass-derived conductive carbon that functions as the catalyst support. The novelty of

this work lies in synthesizing catalyst-support system with a very low loading of noble metal by introducing stacking-faults in Ag nanorings which can transform highly inactive Ag into an efficient HER catalyst. Here, luffa works as a highly porous source of heteroatom-doped carbon with a unique fibro-vascular reticulated structure, providing a highly conductive support for Ag nanorings. The synergy between the anchored high-strain crystals of the Ag nanorings present on the luffa matrix together with the strong chemical interaction between them, provides excellent stability over prolonged periods. This catalyst-support system has the distinct advantage of being simple, economical, and environmentally friendly, where a very low concentration of Ag is sufficient for efficient hydrogen evolution. The as-synthesised Ag/C electrocatalyst requires an overpotential of 116 mV to deliver a current density of 10 mA/cm^2 for hydrogen evolution reaction in an acidic medium, while stable for at least 10 hours of continuous operation. We believe that this concept is not limited to the water splitting application, but also has a potential in synthesis of metal electrocatalysts on mesoporous carbon supports for energy storage, catalysis, carbon capture and chemical looping.

Methodology

Materials:

Materials used in this study include low-density luffa sponge imported from Shenzhen (China), sodium hydroxide, Milli-Q ultrapure water (Millipore, ≥18.2 MΩ cm), 5 wt.% Nafion solution (Merck), absolute ethanol, potassium hydroxide (Extra pure, Fisher Chemicals) potassium chloride (Analytical grade, Fisher Chemicals), and silver nitrate (99.9999%, Merck).

Synthesis:

Due to the way the luffa was harvested, two ends of the luffa were amputated, and the homogeneous cylindrical structure was taken for studies. The core of the cylinder consisted of areas with hardened lignin, which were removed before use. Removal of lignin increases the surface area available for salt impregnation by facilitating fibre separation. The rest of the luffa (hoop region) was cut up into 2×2 cm pieces, washed twice with DI water, and sonicated for 20 mins to remove any dirt build-up. Following several more washing cycles, luffa was soaked in DI water to open up the pores and swell the fibre by water uptake. Raw luffa sponge was pre-treated with 1 M NaOH for 3 hours at 60 °C for cleaning and lignin removal and washed thoroughly with water. The washed sponge was left to dry at ambient conditions before salt impregnation. To form Ag nanorings, luffa was immersed in 0.3 M $AgNO_3$ salt solution for 1 and 5 hrs in a covered beaker, and the solution was slowly stirred at 50 rpm. To keep the mesoporous structure and morphology of luffa intact, the material was taken out and dried by vacuum lyophilisation at -55 °C. Following the drying process, luffa fibres were carbonised in a tube furnace under Ar atmosphere at varying temperatures of 600, 700, 800, 900, 1000 and 1100 °C for 2 hrs with a high heating rate of 8 °C/min to minimise material shrinkage. After holding at peak temperature for 30 minutes, the material was rapidly cooled down to room temperature by passing copious amounts of cool Ar gas (at 4 °C) at a flow rate of 9 L/min through the tube. For microstrain comparison via X-ray diffraction (XRD), a non-strained sample was also synthesized by maintaining all other parameters constant while reducing the argon (Ar) gas flow rate to 2 L/min during the cooling phase. Carbonised luffa fibre (CLF) was then ground to a fine powder using mortar and pestle before being used as a catalyst material.

Characterisation:

Electron microscopy was conducted using a Tecnai F20 transmission electron microscopy (TEM) at an accelerating voltage of 200 keV, attached with an energy dispersive X-ray detector (EDS), as well as a JEOL JSM-6010 scanning electron microscopy (SEM) utilising tungsten cathode microscope, also equipped with an EDS accessory. Raman spectra were obtained using a fully confocal Horiba XploRATM spectrometer (Horiba, Japan) with a green laser (λ = 532 nm) and 50× objective lens. Agilent Cary 360 FT-IR with a diamond ATR module was used to obtain the infrared spectra. Agilent 5800 ICP-OES was used to measure the metal loading on the catalyst system. Surface and chemical bonding characterisations were performed using ESCALAB™ QXi X-ray Photoelectron Spectrometer (XPS) Microprobe by Thermo Fisher Scientific. X-ray diffraction (XRD) studies were performed using Cu Kα radiation on a Siemens D5000 diffractometer from 10-90° with a step width of 0.01° and a counting time of 10 s. The instrument peak broadening was corrected using quartz as the standard reference material.

Electrochemical Test:

The electrochemical measurements were carried out using a three-electrode system in a sealed glass cell with 0.5 M H_2SO_4 electrolyte at 15 °C using an IviumStat electrochemical analyser. A modified glassy carbon electrode (GCE, D=3mm) was used as the working electrode, while Pt wire was used as the counter electrode and an Ag/AgCl electrode with saturated KCl as the reference electrode. Before starting with the measurements, the Ag/AgCl electrode was calibrated each time against a master reference electrode. Obtained potential values were converted from Ag/AgCl to the reversible hydrogen electrode (RHE) using the Nernst equation ($E_{RHE} = E_{Ag/AgCl} + 0.059 \times pH + 0.197$). Polarisation curves were IR-corrected with 90% IR compensation. GCE was polished using standard techniques and electrochemically cleaned before each use. GCE was modified by drop casting the dispersions of catalytic inks. These inks were prepared by mixing 5 mg of the catalyst with 450 µL of IPA, 500 µL of ultrapure water and 50 µL of 5 wt% Nafion D520 solution. The mixture was stirred for 10 mins, followed by sonication for 30 mins to obtain a homogenous ink. A volume of 20 µL from

the prepared ink was applied onto the polished glassy carbon electrode, resulting in a catalyst loading of ~1.4 $mg_{Ag/C}$ cm^{-1}.

Results and discussions

The schematic diagram depicted in Figure 1 illustrates the straightforward approach of employing a solution impregnation and carbonisation technique for the synthesis of the Ag/C catalyst. Commencing this process necessitates the careful selection of a biomass precursor capable of offering a maximum surface area for solution impregnation, producing almost atomically thin carbon walls upon carbonisation, and being readily available and easily processable. In this study, naturally, dried luffa cylindrical fibres (LF) were chosen as the primary candidate owing to their abundant availability and micro-annular structure, which can facilitate the absorption of the Ag-containing solution for the efficient formation of Ag nanoparticles on its surface. Fourier-transform infrared (FT-IR) spectrum of dried LF is shown in Figure S1, with typical C-O, C=O, -CH and -OH functional groups. The application of NaOH treatment was deemed crucial in dissolving any hardened lignin present on the surface, thereby also activating the carbon matrix. This is also supported by the fact that when the washed LF was immersed in water for a few hours, the water surrounding the LF became visually blurry, indicating that the polymeric matrix of LF was experiencing some degree of component loss. Although, it was discovered that the water uptake capacity of the washed LF was marginally higher compared to that treated with NaOH through gravimetric analysis in earlier studies[29], a standardised NaOH pretreatment procedure was adopted to ensure consistency and address these concerns. To understand the physical properties of the biomass substrate, the morphology of NaOH-washed LF without Ag catalyst was first studied by using scanning electron microscopy (SEM) and high-resolution transmission electron microscopy (HR-TEM) for sample prepared by carbonising the LF at 900 °C. As seen in most of the biomass sources, LF produced similar honeycomb structures after carbonisation; where the structural morphology and water uptake in LF results in a 3D architecture composed of very thin interconnected carbon walls with high surface area.

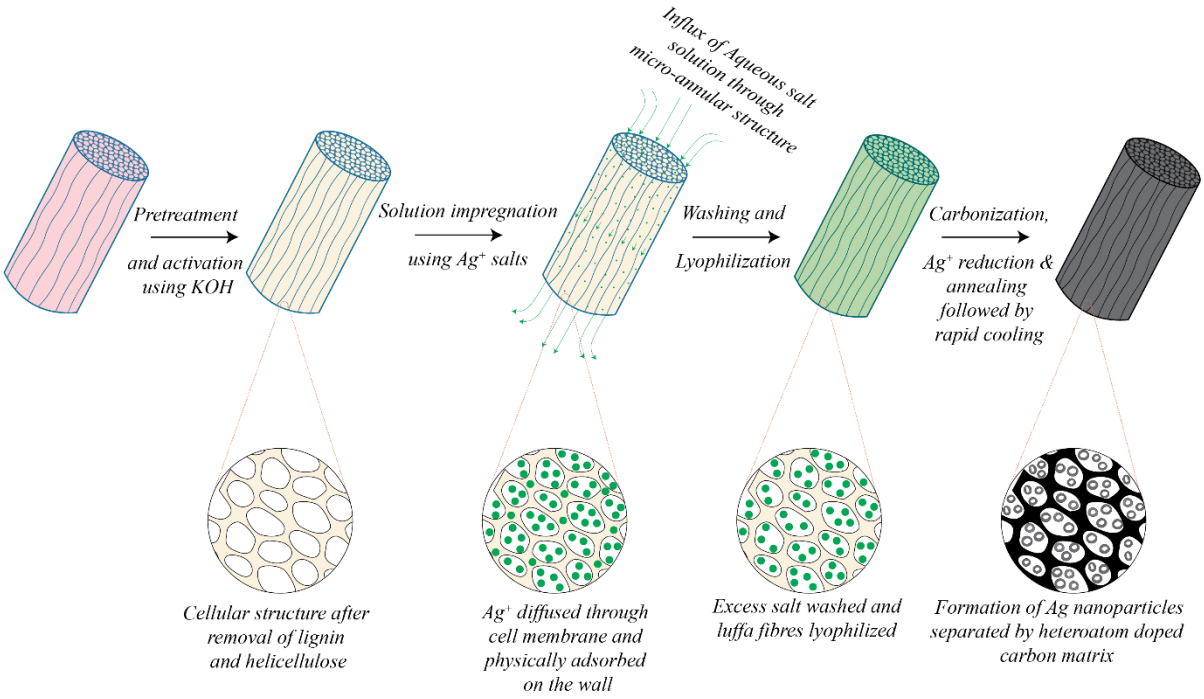

Figure 1. Schematic illustration of the solution impregnation process for synthesizing Ag/C catalyst.

The results, as depicted in Figure 2(a-b), reveal the inherent annular structure of the LF fibres, characterised by a pore diameter ranging from 10 to 20 µm. Upon closer examination of the fibre walls as shown in Figure 2(c), uneven natural deposits became evident, likely originating from hemicellulose and other waxy impurities. A high magnification SEM image recorded on the annular structure can be seen in Figure S2. After undergoing a comprehensive NaOH cleaning and carbonisation process, the overall morphology of carbonised luffa fibre (CLF) resembles that of the non-carbonized material, as shown in Figure 2(d), indicating that the process does not alter the overall structure. However, there is a definite increase in the diameter of the parallel microchannels, which now measure between 20 and 30 µm. This could be attributed to the removal of unwanted natural material deposits both on the outside and inside of the annular structure. Furthermore, a distinct flaky structure became evident upon closer observation of the wall from a lateral perspective, as shown in Figure 2(e), suggesting the formation of atomically thin carbon walls necessary for the catalyst support. The flaky structure is easier to observe when CLF is crushed using a mortar and pestle and then examined using SEM, as shown in Figure S3. Delving deeper into the atomic configuration of this carbon structure using HR-TEM as shown in Figure 2(f), a highly amorphous nature of the

carbon-based material with islands of crystalline carbon arrangement (highlighted by white ovals) can be observed. This suggests a partial graphitisation of the material, possibly responsible for providing increased electrical conductivity to the catalyst support.

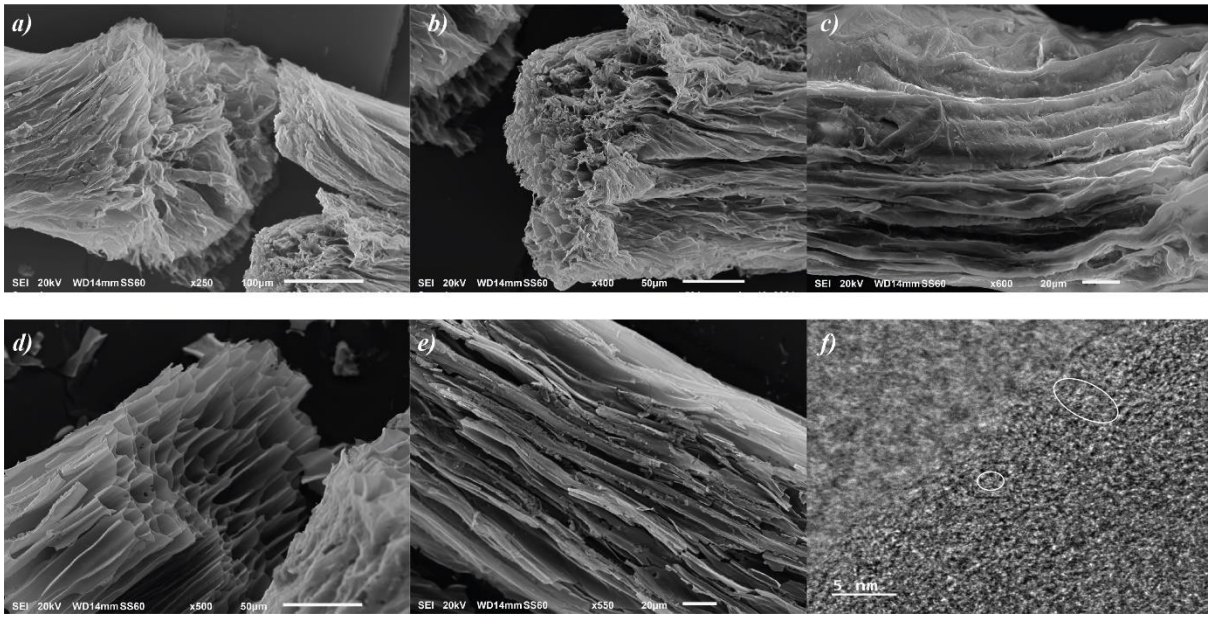

Figure 2. SEM images for a) dried LF cross-section b) magnified image for dried LF cross-section c) LF walls showing ridge like structure due to non-cellulose based components d) cross-sectional image for CLF e) CLF walls showing carbonised flaky structure f) High-resolution transmission electron microscopy (HR-TEM) image for amorphous carbon matrix with graphitic islands as highlighted by circles

Ag/C catalysts were then prepared by using the solution impregnation method as described earlier. After thorough washing of the LF, it was exposed to the solution impregnation for 2 hrs under constant slow stirring and subsequently freeze-dried to obtain Ag^+ infused LF fibres. During the impregnation of Ag^+ into the LF, the Ag^+ ions initially diffuse and permeate through the cell membrane. Subsequently, an ion exchange mechanism takes place between the Ag^+ ions and the cellulose, phospholipid molecules, or membrane proteins present in the cell wall or membrane. This process leads to the discharge of the majority of Ag^+ ions, allowing them to aggregate and form Ag-containing nanoparticles (NPs) that are bonded to the surface of the cell wall and membrane. When the Ag^+ infused LF was sintered at 900 °C under Ar, three processes were likely to happen simultaneously: carbonisation of LF into N-doped carbon support, carbon-assisted reduction of Ag-

containing nanoparticles into metallic Ag nanoparticles in a coordinated ring structure and annealing of Ag nanorings with carbon support.

The morphology and composition of Ag/C were studied after the solution impregnation and carbonisation using SEM, TEM and energy-dispersive X-ray spectroscopy (EDS). The SEM images of the overall surface and single fibre of CLF are shown in Figure 3(a-d), revealing a quite even distribution of ring-like structures across the LF. These nanorings have an average internal diameter of 400 nm and an outer diameter of 800 to 1000 nm. High-magnification SEM micrographs of Figure S4 show the formation of Ag nanorings on significantly thin carbon walls, where Ag nanorings on both sides of the wall can be observed. Conducting a line EDS scan across the ring-like structure, as shown in Figure 3(e), reveals a hollow base, thereby confirming its ring-like nature rather than having a cup morphology, as previously reported.[30] In fact, the LF impregnated for a longer time (10 hours) contained attached spherical clusters instead of ring-like particles, accompanied by a significantly higher loading of Ag, as shown in Figure S5. These observations suggest an enhanced time-dependent diffusion of Ag^+ ions across the plant fibre membrane during the soaking process. The TEM image of a solitary Ag ring on Ag/C, as shown in Figure 3(f), suggests that the ring formation occurs through the Ostwald ripening process. This process involves clustering Ag particles, followed by the annealing of individual Ag nanoparticles (each with a diameter of 30-40 nm) to form the ring structure.[30] A meticulous examination of the ring reveals minute cracks on the surface, which may arise from larger defects or incomplete fusion of crystal boundaries during the annealing process. EDS mapping on the same as shown in Figure 3(g) and EDS spectrum, as shown in Figure S6, further confirm the composition of the structure. The possible mechanism of such an Ostwald ripening process is shown schematically in Figure 4. This uniform and coordinated aggregation of nanoparticles prevents the island formation and results in an even distribution of ring-like structures across the carbon matrix.

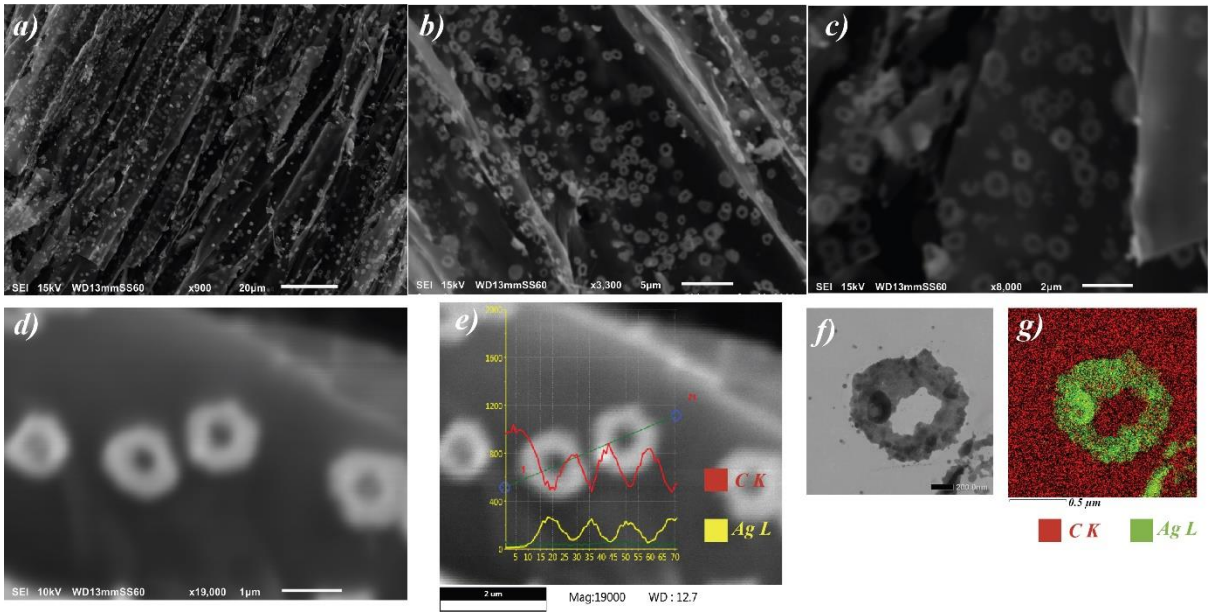

Figure 3. SEM images of a) single CLF strand decorated with Ag nanorings from Ag/C-900 b-d) magnified image for Ag nanorings on Ag/C-900 e) EDS line scan f) TEM image for single Ag structure g) EDS mapping on Fig. 3(f)

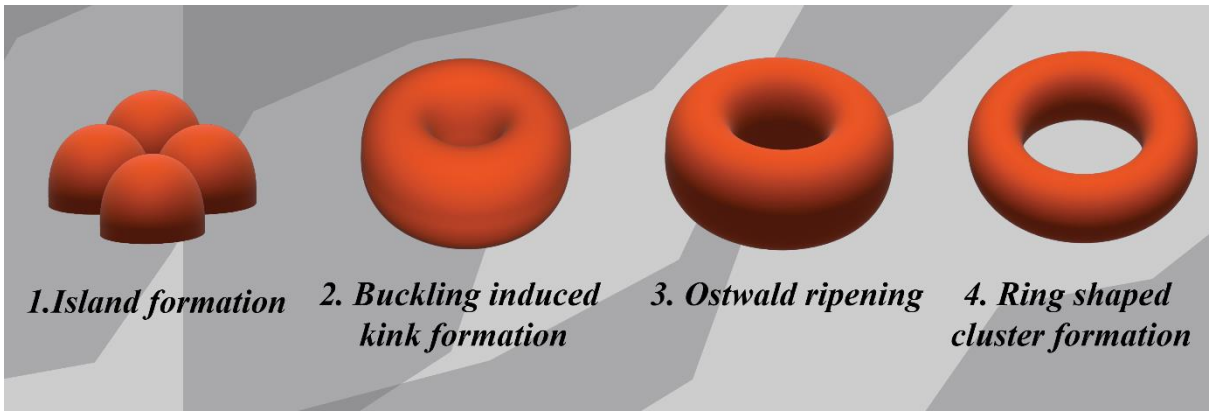

Figure 4. Ostwald ripening model for Ag nanoring formation

To understand the loading of silver on carbon and further probe the surface element composition and valence states of the components, X-ray-photoelectron spectroscopy (XPS) was performed. The XPS survey scan depicted in Figure S7 reveals the presence of Ag, C, N, and O at weight percentages of 2.9, 90.82, 1.94, and 4.34%, respectively, consistent with the Ag total loading observed by EDS and inductively coupled plasma-optical emission spectroscopy (ICP-OES) at around 3% as shown in Table S1. Relatively higher Ag loading can be observed when tested using ICP-OES because XPS

only measures the surface Ag nanoparticles and does not comprise of encapsulated or clustered NPs. The high-resolution photoelectron spectrum of Ag 3d in Figure 5(a) exhibits two distinct peaks at 368.2 and 373.8 eV, corresponding to the Ag $3d_{5/2}$ and $3d_{3/2}$ binding energies of metallic silver, respectively.[31] This observation confirms that the Ag remains in the metallic form and does not undergo significant oxidation. This also means that oxygen present in the system is surface oxygen, bonded mainly to carbon impurities from the environment. The deconvoluted high-resolution XPS spectrum of C 1s in Figure 5(b) shows clear signs of C-C (284.6 eV) corresponding to the sp3 hybridisation of amorphous carbon, C=C (284.3 eV) brought in by the partial graphitisation, C-O/C-N (285.8 eV) which is due to effect of surface oxygen and N-doping of the carbon structure, C=O (288.75 eV) due to surface oxidation and finally π-π* (291.1 eV) shake-up satellite peaks, arising from π-π* type transitions.[32] These transitions involve the promotion of electrons from the highest occupied molecular orbitals (HOMO) to the lowest unoccupied molecular orbitals (LUMO) in the graphitic islands of the C matrix.[33] The N1s spectra in Figure 5(c) can be further deconvoluted into three peaks at 398.6, 400.7 and 401.6 eV, corresponding to the pyridinic-N, pyrrolic-N and graphitic-N, respectively, further confirming the successful doping of N into the carbon matrix.

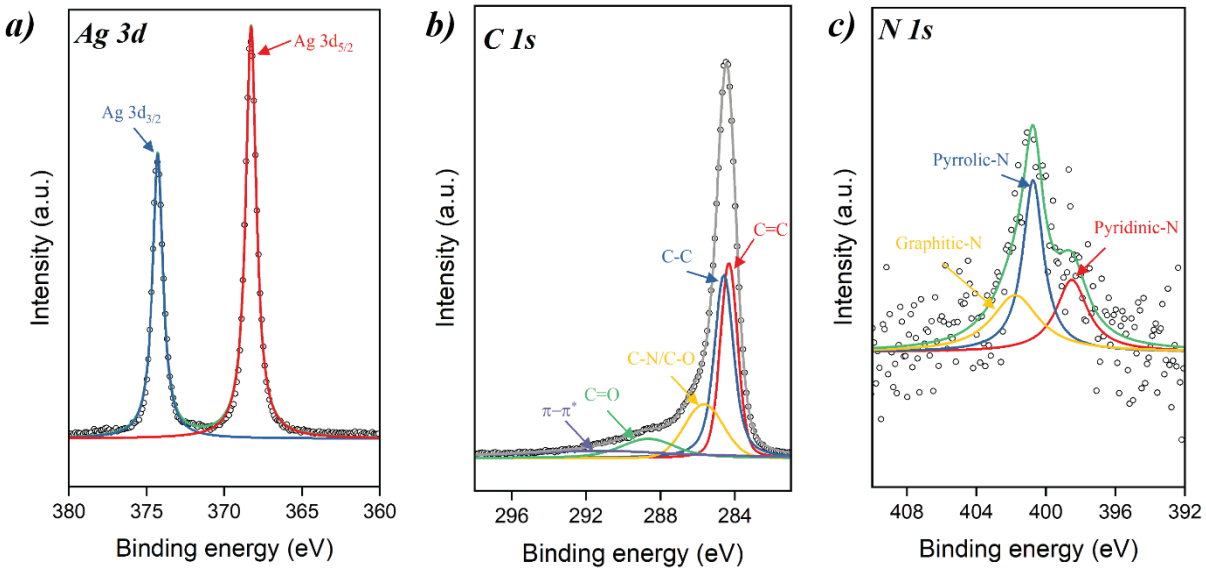

Figure 2. XPS spectra of a) Ag 3d-core level b) C 1s-core level c) N 1s-core level

The Ag/C hybrid was quenched from the carbonisation temperature by creating a significant temperature gradient between the catalyst particles and the surrounding Ar gas. Given the notably low stacking fault energy of Silver (16 mJ m^{-2}) compared to other metals, thermally induced plastic deformation becomes more feasible. This facilitates the generation of stacking faults, as dislocations can readily cross-slip and form stacking faults at localised regions of induced microstrain.

To gain more insights into the crystal deformation experienced by individual Ag nanoparticles and to identify the specific types of faults generated, HR-TEM was utilised. Figure 6 shows an HR-TEM micrograph of the Ag/C catalyst focused on a single nanoparticle that was taken and analysed for structural defects. The micrograph prominently exhibits a profusion of well-defined periodic stacking faults encircling the screw dislocation, initiated through thermal-induced crystal deformation. The swift quenching process instigates the genesis of an abundance of vacancies, which congregate upon the closely packed Ag (111) planes and merge to create stacking faults. Most of the screw dislocations were accompanied by the concurrent presence of edge dislocations. The identification of planes was accomplished by performing an inverse Fast Fourier Transform (FFT) analysis on the HR-TEM micrographs. The resulting data allowed for the allocation of planes based on their corresponding d-spacing values, as demonstrated in Figure 7 (a).

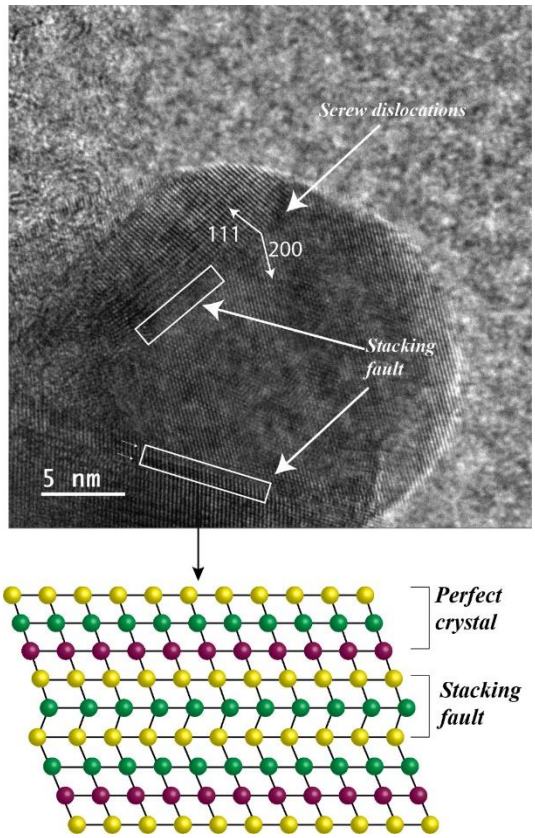

Figure 3. HR-TEM image of Ag single crystal in Ag/C-900 highlighting dislocations.

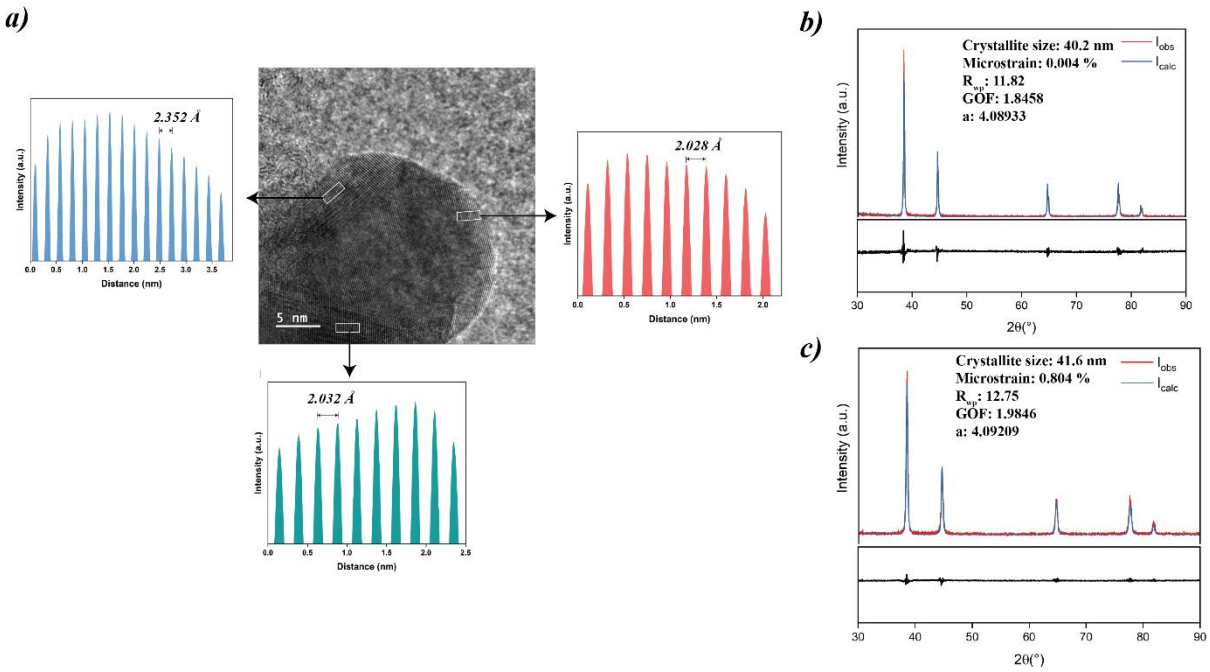

Figure 4. a) allocation of planes by d-spacing measurements on HR-TEM micrograph. XRD pattern with Rietveld refinement for b) Ag/C-900R and c) Ag/C-900. Rwp is the weighted profile R-factor, GOF is the goodness of fit and a is the lattice parameter.

X-ray diffraction (XRD) with Rietveld refinement was utilised to quantify the microstrain in Ag nanoparticles. By adjusting parameters, including microstrain, the analysis provided quantitative information about lattice distortion directly related to the formation of stacking faults in the nanoparticles. A control sample Ag/C-900R was also prepared for Rietveld refinement, where Ag/C was allowed to cool naturally without enhanced cooling effects. Rietveld refinement analysis unveiled a minute microstrain of 0.004% in the Ag nanoparticles, denoting a relatively subdued presence of stacking faults in Ag/C-900R. These findings were echoed in the HR-TEM micrograph showcased in Figure 7(b). In striking contrast, the Ag/C-900 sample as shown in Figure 7(c) unveiled a significantly elevated microstrain of 0.804%, attesting to a pronounced occurrence of stacking faults, as previously observed in the HR-TEM micrograph.

The electrocatalytic performance of the Ag/C-900 catalysts was studied for HER in a standard three-electrode system using a saturated 0.5M H_2SO_4 electrolyte. To begin with, Ag/C-900, Ag/C-600, CLF, and commercially purchased Ag nanoparticles were compared by polarisation curves for HER, as shown in Figure 8(a), where Ag/C-900 exhibits superior performance by a considerable margin. It demonstrated a Tafel slope of 39 mV dec^{-1}, an onset potential at 1 mA cm^{-2} of 77 mV, and an overpotential of 116 mV at 10 mA cm^{-2}, as depicted in Figure 8(b-d). To assess the mechanical stability and adhesion of Ag nanoparticles to the CLF matrix, the electrocatalyst underwent a 2-hour sonication process and subsequent HER testing, showing no significant changes, as illustrated in Figure 8(c). The robust bonding between Ag nanoparticles and the carbon matrix materials offers significant advantages in facilitating electron transfer and ensuring enduring stability in electrocatalytic processes over extended periods. That was further evidenced by testing the Ag/C-900 for long electrochemical cycling. After 10 hours of continuous electrolysis at -0.132 V vs RHE, no significant decay was observed in the current density, as demonstrated in Figure 8(f) and (g).

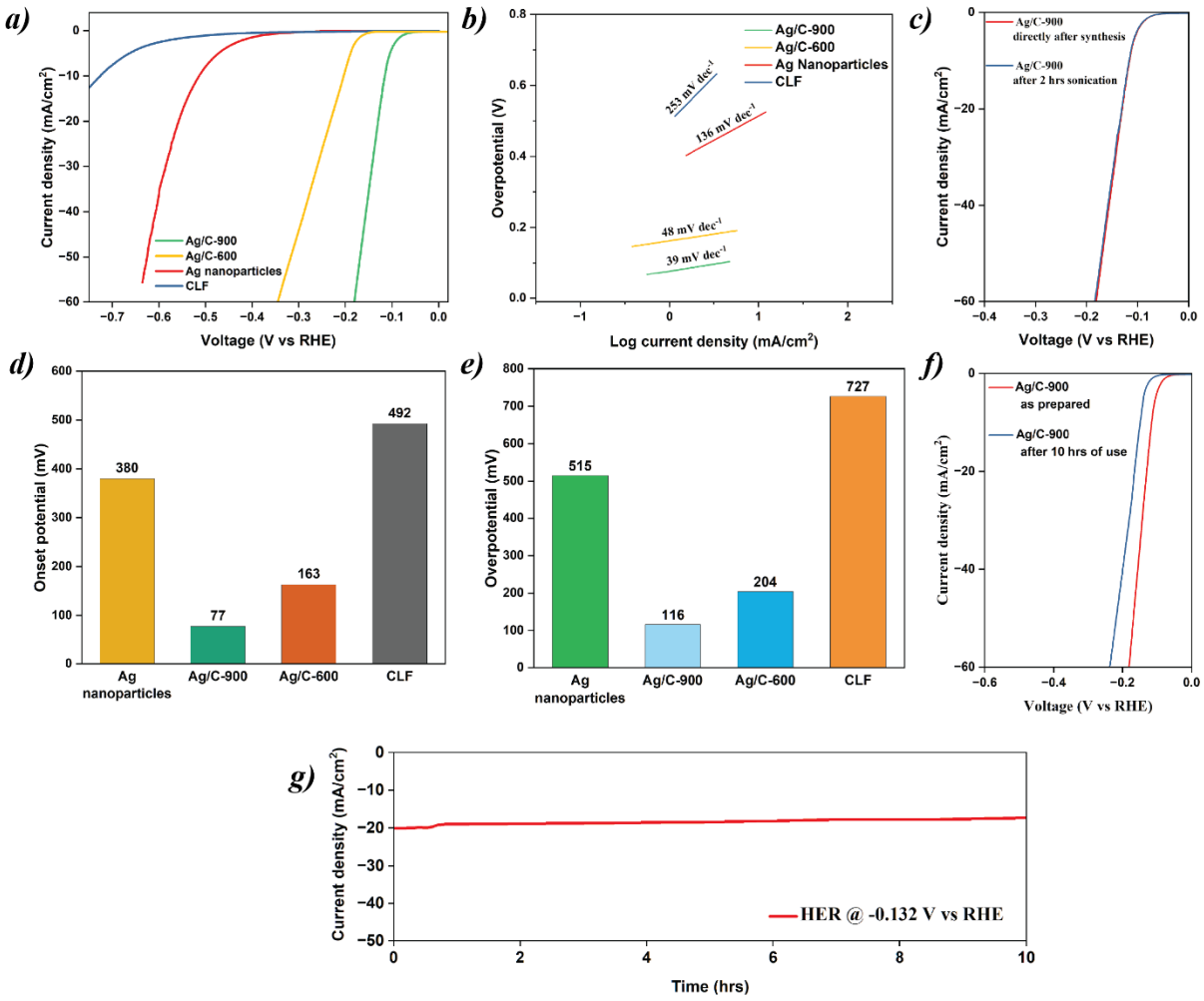

Figure 8. Electrochemical performance of Ag/C-900 catalyst in 0.5 M H2SO4 solution a) HER polarization curves for CLF, commercial Ag nanoparticles, Ag/C-900 and Ag/C-600 b) Tafel slopes from polarization curves c) polarization curves for Ag/C-900 before and after sonication d) comparison for onset potential e) comparison for overpotential f) polarization curves for as prepared catalyst Ag/C-900 and after 10 hrs use g) Chronoamperometric curve for Ag/C-900

To investigate the HER mechanism, Tafel plots were constructed using polarisation curves. The linear region of the Tafel plots, referred to as the kinetically controlled region, was extracted and fitted to the Tafel equation ($\eta = a + b \log j$).[34] The obtained Tafel slopes are 39 mV/dec for Ag/C-900 and 48 mV/dec for Ag/C-600. The hydrogen evolution reaction can occur in the acidic medium through three possible steps.[35] The Volmer step, also known as the discharge step, involves the production of adsorbed hydrogen on the electrocatalyst surface through proton-coupled electron transfer, and the corresponding reaction can be represented by the equation, where the theoretical value of b for this step is approximately 118 mV.

$$Volmer\ step:\ H_3O^+ + e^- + E_c \rightarrow E_C H_{ads} + H_2(g) \qquad (1)$$

After the adsorption of hydrogen, the subsequent desorption process can occur through two possible mechanisms. The first is the Heyrovsky mechanism, where an additional proton from the solution interacts with the adsorbed hydrogen to generate H_2 gas. The theoretical value of b for this mechanism is approximately 39 mV. Alternatively, the desorption can proceed through the Tafel reaction, where two adsorbed hydrogen intermediates recombine. The theoretical value of b for this mechanism is approximately 29.5 mV.

$$Heyrovsky\ step: E_c H_{ads} + H_3O^+ + e^- \rightarrow E_c + H_2O + H_2\,(g) \quad (2)$$

$$Tafel\ step: CH_{ads} + CH_{ads} \rightarrow 2C + H_2\,(g) \quad (3)$$

Our observed Tafel slopes for both Ag/C catalysts, in this case, are around 40 mV/dec, suggesting that the proposed catalysts use the Volmer-Heyrovsky mechanism as the slope of the electrocatalysts is between the theoretical values of corresponding steps. Due to the relatively high Tafel slope, the Heyrovsky step could be the rate-determining step where slower desorption of hydrogen from the surface occurs. However, the reverse scenario in which a limited surface participates in the adsorption of hydrogen, followed by faster hydrogen desorption through the Volmer step, is also possible.

The HER performance of Ag/C catalysts carbonised at different temperatures was investigated, as shown in Figure S8. The catalyst carbonised at 900°C exhibited the highest catalytic activity, indicating that this temperature is optimal for producing efficient structures for electrocatalysts. It is speculated that the enhancement is attributed to the thermally induced structural modifications in the conductive carbon matrix support, for which further spectroscopic and structural studies were performed on the bare carbon support.

Raman spectroscopy was performed to study morphological changes happening to the CLF by changing the carbonisation temperature. Raman spectra of CLF carbonised at different temperatures demonstrate the presence of characteristic broad D and G bands at around 1341 cm^{-1} and 1578 cm^{-1}, respectively, as shown in Figure 9(a), typical for highly disordered hard carbons. D band is associated with the presence of structural defects or disorder in the carbon material. In contrast, the G band

corresponds to the sp^2 hybridisation of carbon atoms in an ordered crystalline lattice.[36] As can be observed, the peaks become sharper with increasing the carbonisation temperature, indicating a significant graphitisation. This is expected since thermal treatment promotes the rearrangement and reordering of carbon atoms, forming more ordered graphitic structures. The shift in the peak position of the D band is noticeable when the carbonisation temperature increases from 600 to 1100 °C, causing the D band to shift from 1363 to 1341 cm^{-1}. Furthermore, the G band in the Raman spectrum shows a redshift, moving towards lower wavelengths, which indicates a reduction in doping and decreased strain within the carbon structure. The increased I_D/I_G ratio with increasing carbonisation temperature as shown in Figure 9(b), coupled with the changes in the D band position and shape, suggest the transformation of defects having large sp^3 islands into smaller types of atomic and linear defects, indicating a gradual progression along the Ferrari amorphisation trajectory. [36, 37] The graphitic nature of the produced carbon at higher temperatures is further evidenced by the detection of the 2D band at ~2681 and ~2684 cm^{-1} for the Ag/C carbonised at 900°C and 1100°C, respectively. This peak shift could possibly suggest a reduction in the number of stacked layers in the nanocrystalline domains of the carbon and the presence of thinner stacks of crystalline carbon in the carbon matrix, with partial oxidation. However, no direct evidence of this was observed by TEM imaging.

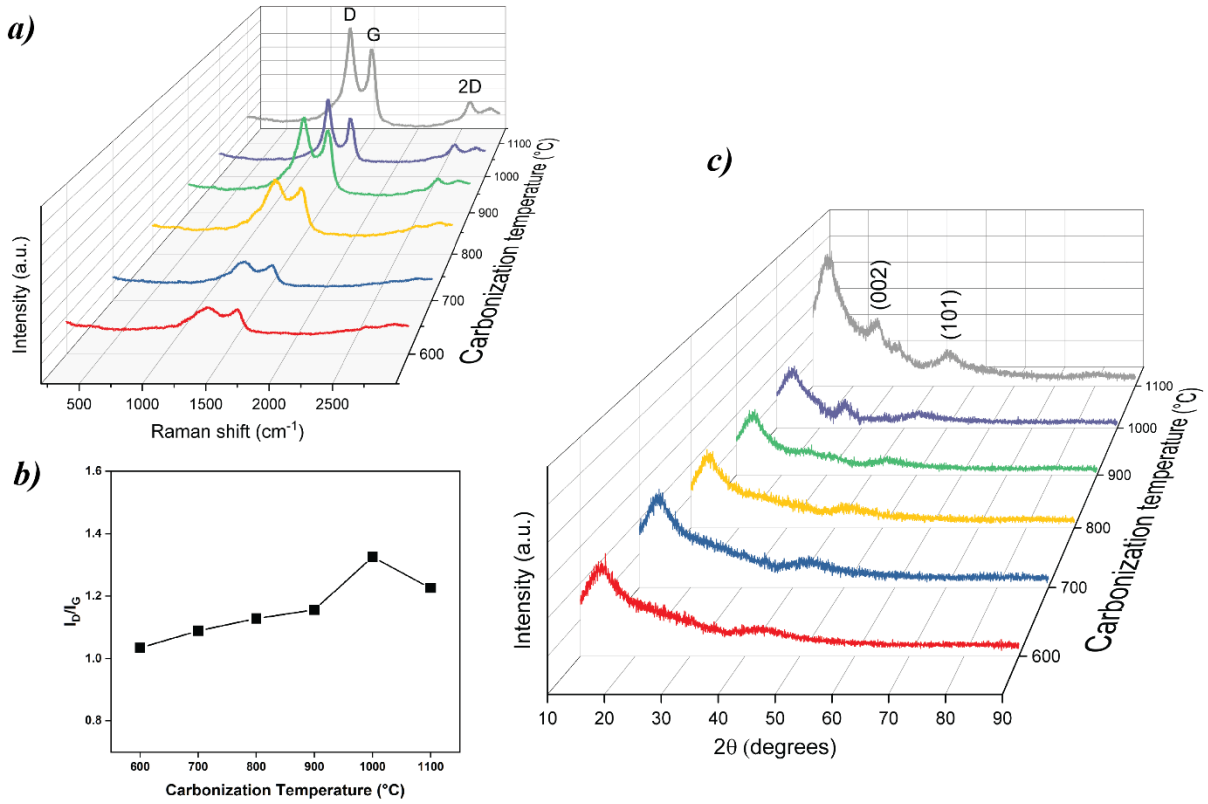

Figure 9. Raman spectroscopy a) Raman spectra of Ag/C catalyst carbonized at different temperature b) comparison of I_D/I_G ratios c) XRD pattern of Ag/C carbonised at various temperatures

The XRD analysis of CLF further confirmed the graphitisation of the LF at high temperatures, as shown in Figure 9(c). Clear development of graphite-related peaks at 2θ = 26.4° and 2θ = 43.1° corresponding to the interplanar distance of d = 3.5 Å and d = 2.1 Å, respectively, can be observed on the XRD pattern. The first peak corresponds to the diffraction on the (002) planes, while the second peak corresponds to the (101) planes. It is worth noting that the (002) direction represents the c-axis of the graphite unit cell, which is perpendicular to the hexagonal planes. Further, the amorphous peak intensity increase at lower 2θ values could also arise from partial oxidation of the nanocrystalline graphitic domains.

Demonstrated in this article, the introduction of crystalline defects and strain to Ag nanorings decorated on luffa-derived carbon structures could provide a driving force to promote the hydrogen evolution reaction, avoiding the requirement for the utilisation of expensive catalysts such as Pt. The tests show the performance of the catalyst is better than many and very much comparable to the best works in this area as shown in Table S2. Future research may focus on the impact of crystalline

defects/strain at various levels and configurations on the catalytic activity of the system in more details.

Conclusion

A straightforward strategy was demonstrated to leverage the synergistic properties of metal-carbon structures for efficient hydrogen evolution. The introduction of stacking faults into Ag crystalline structure, in combination with the electron transfer characteristics of highly conductive biomass-derived carbon support, enable the creation of a highly efficient electrocatalyst for the HER, achievable while using a minimal amount of metal nanoparticles. This modification effectively transforms previously inactive or poorly active Ag into a highly efficient catalyst for HER through the utilisation of an environmentally friendly carbon precursor, ultimately enhancing the overall performance of the electrocatalyst. Furthermore, we have investigated the impact of carbonisation temperature on the properties of the carbon backbone to comprehend its influence on HER activity. This novel concept opens up a new avenue for the synthesis of more straightforward electrocatalysts with significantly reduced metal loadings for HER and other electrocatalytic applications.

Supporting Information

Elemental composition measured by different techniques, FT-IR of natural LF, SEM images of LF at different stages of the process, SEM images of spherical Ag clusters, EDS spectrum, XPS survey scan, Polarization curves of Ag/C processed at different temperatures, Comparison of HER performance from literature.

Acknowledgements

This research was supported by the funding from the British Council through Going Global Partnerships grant.

References

(1) Jacobson, M. Z.; Colella, W. G.; Golden, D. M. Cleaning the Air and Improving Health with Hydrogen Fuel-Cell Vehicles. *Science* **2005**, *308* (5730), 1901-1905. DOI: doi:10.1126/science.1109157.

(2) Lee, D.-Y.; Elgowainy, A. By-Product Hydrogen from Steam Cracking of Natural Gas Liquids (Ngls): Potential for Large-Scale Hydrogen Fuel Production, Life-Cycle Air Emissions Reduction, and Economic Benefit. *International Journal of Hydrogen Energy* **2018**, *43* (43), 20143-20160. DOI: https://doi.org/10.1016/j.ijhydene.2018.09.039.

(3) Li, G.; Han, G.; Wang, L.; Cui, X.; Moehring, N. K.; Kidambi, P. R.; Jiang, D.-e.; Sun, Y. Dual Hydrogen Production from Electrocatalytic Water Reduction Coupled with Formaldehyde Oxidation via a Copper-Silver Electrocatalyst. *Nature Communications* **2023**, *14* (1), 525. DOI: 10.1038/s41467-023-36142-7.

(4) Wang, S.; Lu, A.; Zhong, C.-J. Hydrogen Production from Water Electrolysis: Role of Catalysts. *Nano Convergence* **2021**, *8* (1), 4. DOI: 10.1186/s40580-021-00254-x.

(5) Jiao, Y.; Zheng, Y.; Jaroniec, M.; Qiao, S. Z. Design of Electrocatalysts for Oxygen- and Hydrogen-Involving Energy Conversion Reactions. *Chemical Society Reviews* **2015**, *44* (8), 2060-2086, 10.1039/C4CS00470A. DOI: 10.1039/C4CS00470A.

(6) Zheng, Y.; Jiao, Y.; Jaroniec, M.; Qiao, S. Z. Advancing the Electrochemistry of the Hydrogen-Evolution Reaction Through Combining Experiment and Theory. *Angewandte Chemie International Edition* **2015**, *54* (1), 52-65. DOI: https://doi.org/10.1002/anie.201407031.

(7) Gerber, I. C.; Serp, P. A Theory/Experience Description of Support Effects in Carbon-Supported Catalysts. *Chemical Reviews* **2020**, *120* (2), 1250-1349. DOI: 10.1021/acs.chemrev.9b00209.

(8) Liu, S.; Shen, Y.; Zhang, Y.; Cui, B.; Xi, S.; Zhang, J.; Xu, L.; Zhu, S.; Chen, Y.; Deng, Y.; et al. Extreme Environmental Thermal Shock Induced Dislocation-Rich Pt Nanoparticles Boosting Hydrogen Evolution Reaction. *Advanced Materials* **2022**, *34* (2), 2106973. DOI: https://doi.org/10.1002/adma.202106973.

(9) Zeng, Z.; Küspert, S.; Balaghi, S. E.; Hussein, H. E. M.; Ortlieb, N.; Knäbbeler-Buß, M.; Hügenell, P.; Pollitt, S.; Hug, N.; Melke, J.; et al. Ultrahigh Mass Activity Pt Entities Consisting of Pt Single atoms, Clusters, and Nanoparticles for Improved Hydrogen Evolution Reaction. *Small* **2023**, *19* (29), 2205885. DOI: https://doi.org/10.1002/smll.202205885.

(10) Uchida, T.; Mogami, H.; Yamakata, A.; Sasaki, Y.; Osawa, M. Hydrogen Evolution Reaction Catalyzed by Proton-Coupled Redox Cycle of 4,4′-Bipyridine Monolayer Adsorbed on Silver Electrodes. *J Am Chem Soc* **2008**, *130* (33), 10862-10863. DOI: 10.1021/ja803446s.

(11) Khorshidi, A.; Violet, J.; Hashemi, J.; Peterson, A. A. How Strain Can Break the Scaling Relations of Catalysis. *Nature Catalysis* **2018**, *1* (4), 263-268. DOI: 10.1038/s41929-018-0054-0.

(12) Qu, Y.; Chen, B.; Li, Z.; Duan, X.; Wang, L.; Lin, Y.; Yuan, T.; Zhou, F.; Hu, Y.; Yang, Z.; et al. Thermal Emitting Strategy to Synthesize Atomically Dispersed Pt Metal Sites from Bulk Pt Metal. *Journal of the American Chemical Society* **2019**, *141* (11), 4505-4509. DOI: 10.1021/jacs.8b09834.

(13) Anantharaj, S.; Karthik, P. E.; Subramanian, B.; Kundu, S. Pt Nanoparticle Anchored Molecular Self-Assemblies of DNA: An Extremely Stable and Efficient HER Electrocatalyst with Ultralow Pt Content. *ACS Catalysis* **2016**, *6* (7), 4660-4672. DOI: 10.1021/acscatal.6b00965.

(14) Li, J.; Liu, H.-X.; Gou, W.; Zhang, M.; Xia, Z.; Zhang, S.; Chang, C.-R.; Ma, Y.; Qu, Y. Ethylene-Glycol Ligand Environment Facilitates Highly Efficient Hydrogen Evolution Of Pt/CoP Through Proton Concentration and Hydrogen Spillover. *Energy & Environmental Science* **2019**, *12* (7), 2298-2304, 10.1039/C9EE00752K. DOI: 10.1039/C9EE00752K.

(15) Li, K.; Li, Y.; Wang, Y.; Ge, J.; Liu, C.; Xing, W. Enhanced Electrocatalytic Performance for the Hydrogen Evolution Reaction Through Surface Enrichment of Platinum Nanoclusters Alloying with Ruthenium In Situ Embedded In Carbon. *Energy & Environmental Science* **2018**, *11* (5), 1232-1239, 10.1039/C8EE00402A. DOI: 10.1039/C8EE00402A.

(16) Wang, J.; Xu, F.; Jin, H.; Chen, Y.; Wang, Y. Non-Noble Metal-based Carbon Composites in Hydrogen Evolution Reaction: Fundamentals to Applications. *Advanced Materials* **2017**, *29* (14), 1605838. DOI: https://doi.org/10.1002/adma.201605838.
(17) Chen, S.; Min, X.; Zhao, Y.; Wu, X.; Zhang, D.; Hou, X.; Wu, X.; Liu, Y. g.; Huang, Z.; Abdelkader, A. M.; et al. Nickel Quantum Dots Anchored in Biomass-Derived Nitrogen-Doped Carbon as Bifunctional Electrocatalysts for Overall Water Splitting. *Advanced Materials Interfaces* **2022**, *9* (7), 2102014. DOI: https://doi.org/10.1002/admi.202102014.
(18) Fan, L.; Liu, P. F.; Yan, X.; Gu, L.; Yang, Z. Z.; Yang, H. G.; Qiu, S.; Yao, X. Atomically Isolated Nickel Species Anchored on Graphitized Carbon for Efficient Hydrogen Evolution Electrocatalysis. *Nature Communications* **2016**, *7* (1), 10667. DOI: 10.1038/ncomms10667.
(19) Fei, H.; Dong, J.; Arellano-Jiménez, M. J.; Ye, G.; Dong Kim, N.; Samuel, E. L. G.; Peng, Z.; Zhu, Z.; Qin, F.; Bao, J.; et al. Atomic Cobalt on Nitrogen-Doped Graphene for Hydrogen Generation. *Nature Communications* **2015**, *6* (1), 8668. DOI: 10.1038/ncomms9668.
(20) Zhang, L.; Liu, W.; Dou, Y.; Du, Z.; Shao, M. The Role of Transition Metal and Nitrogen in Metal–N–C Composites for Hydrogen Evolution Reaction at Universal pHs. *The Journal of Physical Chemistry C* **2016**, *120* (51), 29047-29053. DOI: 10.1021/acs.jpcc.6b11782.
(21) Liu, H.; Jin, M.; Zhan, D.; Wang, J.; Cai, X.; Qiu, Y.; Lai, L. Stacking Faults Triggered Strain Engineering of ZIF-67 Derived Ni-Co Bimetal Phosphide for Enhanced Overall Water Splitting. *Applied Catalysis B: Environmental* **2020**, *272*, 118951. DOI: https://doi.org/10.1016/j.apcatb.2020.118951.
(22) Fang, L.; Lu, S.; Liu, H. Electrocatalytic Nitrate Reduction to Ammonia By Oxide-Derived Copper with Stacking Faults. *ECS Meeting Abstracts* **2022**, *MA2022-02* (54), 2031. DOI: 10.1149/MA2022-02542031mtgabs.
(23) Zhu, Q.; Pan, Z.; Zhao, Z.; Cao, G.; Luo, L.; Ni, C.; Wei, H.; Zhang, Z.; Sansoz, F.; Wang, J. Defect-Driven Selective Metal Oxidation at Atomic Scale. *Nature Communications* **2021**, *12* (1), 558. DOI: 10.1038/s41467-020-20876-9.
(24) Poerwoprajitno, A. R.; Gloag, L.; Watt, J.; Cheong, S.; Tan, X.; Lei, H.; Tahini, H. A.; Henson, A.; Subhash, B.; Bedford, N. M.; et al. A Single-Pt-Atom-On-Ru-Nanoparticle Electrocatalyst For CO-Resilient Methanol Oxidation. *Nature Catalysis* **2022**, *5* (3), 231-237. DOI: 10.1038/s41929-022-00756-9.
(25) Poerwoprajitno, A. R.; Gloag, L.; Cheong, S.; Gooding, J. J.; Tilley, R. D. Synthesis of Low- and High-Index Faceted Metal (Pt, Pd, Ru, Ir, Rh) Nanoparticles for Improved Activity and Stability in Electrocatalysis. *Nanoscale* **2019**, *11* (41), 18995-19011, 10.1039/C9NR05802H. DOI: 10.1039/C9NR05802H.
(26) Li, Z.; Fu, J.-Y.; Feng, Y.; Dong, C.-K.; Liu, H.; Du, X.-W. A Silver Catalyst Activated by Stacking Faults for the Hydrogen Evolution Reaction. *Nature Catalysis* **2019**, *2* (12), 1107-1114. DOI: 10.1038/s41929-019-0365-9.
(27) Ramadhan, Z. R.; Poerwoprajitno, A. R.; Cheong, S.; Webster, R. F.; Kumar, P. V.; Cychy, S.; Gloag, L.; Benedetti, T. M.; Marjo, C. E.; Muhler, M.; et al. Introducing Stacking Faults into Three-Dimensional Branched Nickel Nanoparticles for Improved Catalytic Activity. *J Am Chem Soc* **2022**, *144* (25), 11094-11098. DOI: 10.1021/jacs.2c04911.
(28) Jiang, R.; Da, Y.; Zhang, J.; Wu, H.; Fan, B.; Li, J.; Wang, J.; Deng, Y.; Han, X.; Hu, W. Non-Equilibrium Synthesis of Stacking Faults-Abundant Ru Nanoparticles Towards Electrocatalytic Water Splitting. *Applied Catalysis B: Environmental* **2022**, *316*, 121682. DOI: https://doi.org/10.1016/j.apcatb.2022.121682.
(29) Zhang, K.; Guo, Y.; Yuan, F.; Zhang, T.; Zhu, Z.; Weng, B.; Wu, S.; Chen, T.; Chen, Y. Effect of Chemical Treatments on the Properties of High-Density Luffa Mattress Filling Materials. *Materials* **2019**, *12* (11), 1796.
(30) Mishra, Y. K.; Adelung, R.; Kumar, G.; Elbahri, M.; Mohapatra, S.; Singhal, R.; Tripathi, A.; Avasthi, D. K. Formation of Self-organized Silver Nanocup-Type Structures and Their Plasmonic Absorption. *Plasmonics* **2013**, *8* (2), 811-815. DOI: 10.1007/s11468-013-9477-2.

(31) Vasil'kov, A.; Batsalova, T.; Dzhambazov, B.; Naumkin, A. XPS Study of Silver and Copper Nanoparticles Demonstrated Selective Anticancer, Proapoptotic, And Antibacterial Properties. *Surface and Interface Analysis* **2022**, *54* (3), 189-202. DOI: https://doi.org/10.1002/sia.7038.
(32) Chen, X.; Wang, X.; Fang, D. A Review on C1s XPS-Spectra for Some Kinds of Carbon Materials. *Fullerenes, Nanotubes and Carbon Nanostructures* **2020**, *28* (12), 1048-1058. DOI: 10.1080/1536383X.2020.1794851.
(33) Speranza, G. Characterization of Carbon Nanostructures by Photoelectron Spectroscopies. *Materials* **2022**, *15* (13), 4434.
(34) Seri, O. Differentiating Approach to the Tafel Slope of Hydrogen Evolution Reaction on Nickel Electrode. *Electrochemistry Communications* **2017**, *81*, 150-153. DOI: https://doi.org/10.1016/j.elecom.2017.07.004.
(35) Prats, H.; Chan, K. The Determination of the HOR/HER Reaction Mechanism from Experimental Kinetic Data. *Physical Chemistry Chemical Physics* **2021**, *23* (48), 27150-27158, 10.1039/D1CP04134G. DOI: 10.1039/D1CP04134G.
(36) Ferrari, A. C.; Robertson, J. Interpretation of Raman Spectra of Disordered and Amorphous Carbon. *Physical Review B* **2000**, *61* (20), 14095-14107. DOI: 10.1103/PhysRevB.61.14095.
(37) Xu, Z.; Guo, Z.; Madhu, R.; Xie, F.; Chen, R.; Wang, J.; Tebyetekerwa, M.; Hu, Y.-S.; Titirici, M.-M. Homogenous Metallic Deposition Regulated by Defect-Rich Skeletons for Sodium Metal Batteries. *Energy & Environmental Science* **2021**, *14* (12), 6381-6393, 10.1039/D1EE01346G. DOI: 10.1039/D1EE01346G.